PAPER

Analysis of dislocation defects in compositionally step-graded α-(Al$_x$Ga$_{1−x}$)$_2$O$_3$ layers

Tatsuya Yasuoka,[a] Hiromu Susami,[a] Li Liu, [ID][ab] Giang T. Dang[ab] and Toshiyuki Kawaharamura*[ab]

The ultra-wide bandgap semiconductor α-Ga$_2$O$_3$ can be heteroepitaxially grown on a sapphire substrate. However, due to a lattice mismatch of about 4.6% with a sapphire substrate, many dislocation defects occur in α-Ga$_2$O$_3$ films. To reduce the dislocation density, compositionally step-graded α-(Al$_x$Ga$_{1−x}$)$_2$O$_3$ layers were fabricated on a *c*-plane sapphire substrate using mist CVD. TEM measurements revealed few dislocations in the initial layer of α-(Al$_{0.96}$Ga$_{0.04}$)$_2$O$_3$, but numerous dislocations were observed in the subsequent layer of α-(Al$_{0.84}$Ga$_{0.16}$)$_2$O$_3$. However, the step-graded α-(Al$_x$Ga$_{1−x}$)$_2$O$_3$ layers exhibited bending of the dislocations under both compressive and tensile strains due to compositional differences of α-(Al$_x$Ga$_{1−x}$)$_2$O$_3$, resulting in about 50% reduction of the dislocation density in the high-Ga-composition layer of α-(Al$_x$Ga$_{1−x}$)$_2$O$_3$. The introduction of multiple 50 nm α-Ga$_2$O$_3$ layers into the compositionally step-graded α-(Al$_x$Ga$_{1−x}$)$_2$O$_3$ layers resulted in a notable reduction in dislocation defects at the interface between the sandwiched α-Ga$_2$O$_3$ layers. It is assumed that the dislocations were bent by the strain caused by the composition change, resulting in a decrease in the number of dislocations. It is anticipated that further reduction of dislocation density will be achieved by optimizing the composition change and thicknesses of layers that provide effective strain for dislocation bending, and by stacking these layers.

1. Introduction

Gallium oxide (Ga$_2$O$_3$) is gaining attention as an ultra-wide bandgap semiconductor material. Ga$_2$O$_3$ has various crystal structures,[1] and among them, the thermally most stable phase is β-Ga$_2$O$_3$ with a band gap of ~4.9 eV,[2,3] which can be grown from melt.[4–7] Thus, homoepitaxial growth is possible,[8–10] and β-Ga$_2$O$_3$ has been the most actively studied. On the other hand, α-Ga$_2$O$_3$, which has a corundum structure and is thermally metastable, has the largest band gap of 5.3 eV (ref. 11) (5.61 eV),[12] among Ga$_2$O$_3$ polymorphs of different crystal structures and can be heteroepitaxially grown on a sapphire substrate.[11,13–18] It can be mixed with other corundum-structured oxides α-(M$_x$Ga$_{1−x}$)$_2$O$_3$ [M = Al,[19–24] In,[25] Fe,[26] Cr,[27] and Ir[28]] to control various properties such as band gaps and lattice constants, and is expected to be used for power devices. However, the sapphire substrate and α-Ga$_2$O$_3$ have about 4.60% lattice mismatch along the *a*-axis,[29] and many dislocations are formed due to this large lattice mismatch.[30,31] This high dislocation density is one of the most significant problems to be solved in α-Ga$_2$O$_3$ device applications. Previous studies have

examined the Epitaxial Lateral Overgrowth (ELO) method[32–35] and the introduction of α-(Al$_x$Ga$_{1−x}$)$_2$O$_3$ buffer layers[20,36,37] to decrease dislocation density. In this study, we have attempted to fabricate compositionally step-graded α-(Al$_x$Ga$_{1−x}$)$_2$O$_3$ layers to reduce the dislocation density. Additionally, in a previous study, the dislocation density was reduced with the introduction of quasi-graded α-(Al$_x$Ga$_{1−x}$)$_2$O$_3$ buffer layers, although the mechanism behind it was unclear.[36] This study revealed the mechanism by analyzing dislocations in the step-graded α-(Al$_x$Ga$_{1−x}$)$_2$O$_3$ layers.

2. Experimental details

To fabricate compositionally step-graded α-(Al$_x$Ga$_{1−x}$)$_2$O$_3$ layers, it is necessary to determine the growth rate for each α-(Al$_x$Ga$_{1−x}$)$_2$O$_3$ composition. Therefore, several α-(Al$_x$Ga$_{1−x}$)$_2$O$_3$ thin films with different compositions were grown and their growth rates were investigated. The growth conditions are summarized in Table 1. Gallium(III) acetylacetonate (Ga(acac)$_3$) and aluminum(III) acetylacetonate (Al(acac)$_3$) were used as precursors for Ga and Al, respectively. They were dissolved in a mixture of deionized water and hydrochloric acid (HCl) at concentrations of 20 mM and 40 mM, respectively. A schematic diagram of the mist CVD system used for α-(Al$_x$Ga$_{1−x}$)$_2$O$_3$ growth in this work is shown in Fig. 1. Mist generated by the ultrasonic transducers from each solution chamber was well mixed in a dedicated

*a*School of Systems Engineering, Kochi University of Technology, 185 Miyanokuchi, Tosayamada, Kami, Kochi, 782-8502, Japan

*b*Center for Nanotechnology, Research Institute, Kochi University of Technology, 185 Miyanokuchi, Tosayamada, Kami, Kochi 782-8502, Japan. E-mail: kawaharamura. toshiyuki@kochi-tech.ac.jp

Table 1 Growth conditions of α-$(Al_xGa_{1-x})_2O_3$ thin films

| Solution	A	B
Solute	Ga(acac)$_3$[a]	Al(acac)$_3$[b]
Concentration	20 mM	40 mM
Solvent (mixing ratio)	DI water[c] : HCl[d] (199 : 1)	
Gas	N$_2$	
Substrate	c-Plane sapphire	
Growth temperature	450 °C	
Growth system	3G mist CVD	
Ultrasonic transducer	2.4 MHz, 24 V–0.625 A ($\times$3)	

[a] Gallium acetylacetonate, 99.99%, Sigma-Aldrich. [b] Aluminum acetylacetonate, 99.99%, Sigma-Aldrich. [c] De-ionized water, Merck Millipore. [d] Hydrochloric acid, 35–37%, Wako Pure Chemical Corporation.
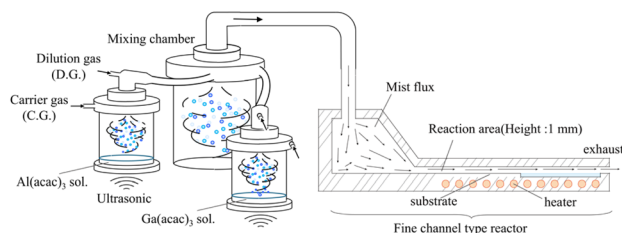
**Fig. 1** A schematic diagram of the 3G mist CVD system.

mixing chamber and then supplied to a fine channel reactor. Details of this mist CVD system were described in ref. 38–42. Nitrogen was used as carrier and dilution gases, and α-$(Al_xGa_{1-x})_2O_3$ thin films of different compositions were grown by changing the ratio of Al/Ga carrier gas flow rates. Dilution gas flows were adjusted accordingly to maintain a total flow rate of 6.0 L min^{-1} for each solution chamber, resulting in a total flow rate of 12 L min^{-1} in the reactor. α-$(Al_xGa_{1-x})_2O_3$ thin films were grown on c-plane sapphire substrates at 450 °C.

3. Results and discussion

The XRD spectra are shown in Fig. 2. The peaks in the range of 40.3–41.7° correspond α-$(Al_xGa_{1-x})_2O_3$ (0006), and the peak at around 38.9° corresponds to ε-Ga_2O_3 (004). The origin of the peak at 41.9° remains unidentified. The peak corresponding to α-$(Al_xGa_{1-x})_2O_3$ (0006) shifted towards the high-angle side as the carrier gas ratio of Al increased, suggesting that the composition of α-$(Al_xGa_{1-x})_2O_3$ could be readily controlled. The α-$(Al_xGa_{1-x})_2O_3$ composition ratio in the film was determined by analyzing the peak positions, as Vegard's law applies to α-$(Al_xGa_{1-x})_2O_3$.[19] Additionally, the thickness of each α-$(Al_xGa_{1-x})_2O_3$ film was determined by the fringe spacing. The summarized dependencies of composition ratios and growth rates on carrier gas ratios are shown in Fig. 3. Although the thickness of the α-$(Al_xGa_{1-x})_2O_3$ film, which was grown using a carrier gas ratio of Al/Ga = 2.0/3.0 L min^{-1}, could not be calculated due to unclear fringes, it was found that the growth rate can be approximated linearly with the Al/Ga carrier gas ratio under the present growth conditions.
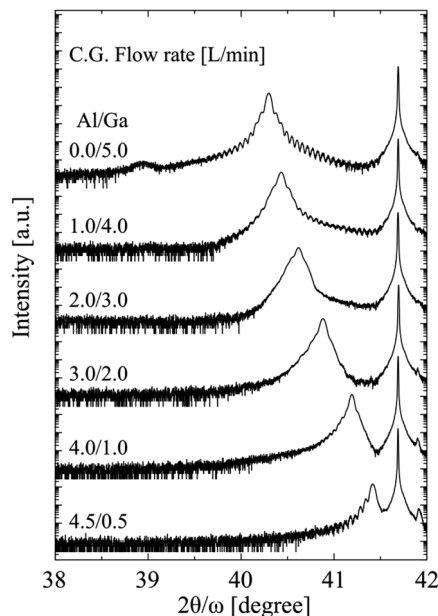
Fig. 2 XRD spectra of α-$(Al_xGa_{1-x})_2O_3$ thin films grown by different Al/Ga carrier gas ratio.

Next, Fig. 4 shows the schematic diagram of the fabricated compositionally step-graded α-$(Al_xGa_{1-x})_2O_3$ layers. The Al carrier gas was decreased by 0.2 L min^{-1} from 4.8 to 0.0 L min^{-1}, and the Ga carrier gas was increased by 0.2 L min^{-1} from 0.2 to 5.0 L min^{-1}, so that the composition gradually changed from α-Al_2O_3 to α-Ga_2O_3, forming a total of 25 layers. Table 2 summarizes the carrier gas flow rates and actual film thicknesses of all layers. The thicknesses were equal to or thicker than 50 nm and the growth times were determined based on the results in Fig. 3. α-$(Al_xGa_{1-x})_2O_3$ layers with high Al compositions were thicker than 50 nm due to the presence of compressive strains observed in the high-Al compositions, whereas other layers were 50 nm thick. To grow this structure, the Al and Ga precursor solutions used were the same as those listed in Table 1. Prior to the growth, the c-plane sapphire
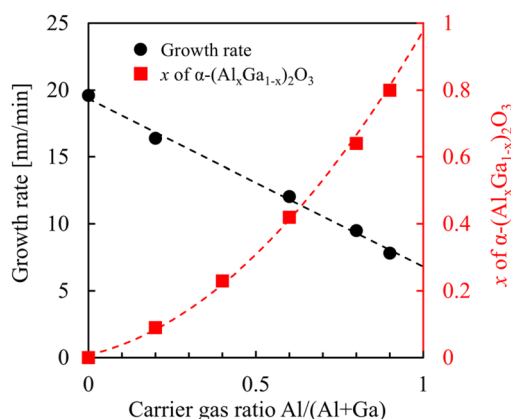
Fig. 3 Dependences of growth rates and composition ratios x of α-$(Al_xGa_{1-x})_2O_3$ on carrier gas ratio Al/(Al + Ga).

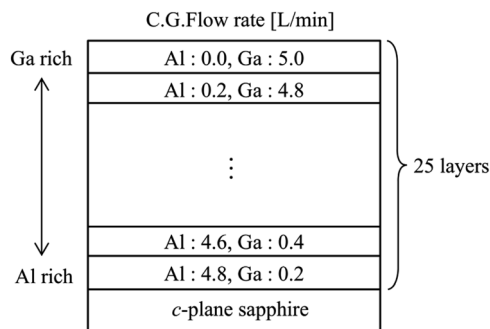**Fig. 4** A schematic diagram of the fabricated compositionally step-graded α-$(Al_xGa_{1-x})_2O_3$ layers.

Table 2 Carrier gas conditions of compositionally step-graded α-$(Al_xGa_{1-x})_2O_3$ layers

Layer	Thickness (nm)	Carrier gas flow rate	
		Al (L min^{-1})	Ga (L min^{-1})
1	80	4.8	0.2
2	75	4.6	0.4
3	70	4.4	0.6
4	65	4.2	0.8
5	60	4.0	1.0
6	58	3.8	1.2
7	56	3.6	1.4
8	54	3.4	1.6
9	52	3.2	1.8
10	50	3.0	2.0
	50	**Decrease by 0.2**	**Increase by 0.2**
25	50	0.0	5.0

substrate was immersed in a 5 : 2 solution of sulfuric acid and hydrogen peroxide for 10 minutes, followed by a further rinse in deionized water for at least 10 minutes.

Fig. 5 shows reciprocal space mapping around the $(10\bar{1},10)$ reflection and the dashed line in the figure connects the ideal
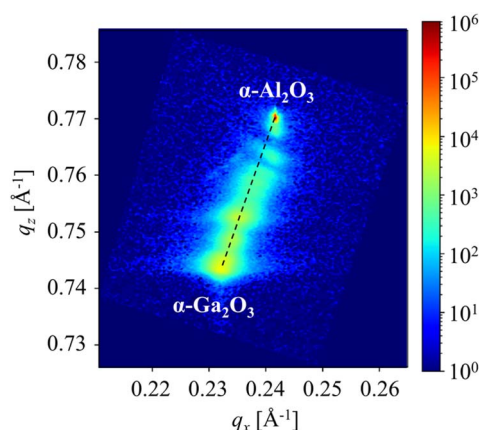
peak positions of α-Al_2O_3 (q_x: 0.243, q_z: 0.770) and α-Ga_2O_3 (q_x: 0.232, q_z: 0.744).[43] The peak near the reflection from the sapphire substrate did not follow the dashed line, indicating that high-Al-composition layers seem to have been subjected to a slight in-plane compressive strain. This suggests that a large lattice mismatch occurred between the layer under compressive strain and the relaxed layer. In contrast, in other regions, peaks were observed along the dashed line, indicating that α-$(Al_xGa_{1-x})_2O_3$ layers were fully relaxed.

Fig. 6(a) shows a cross-sectional high-angle annular dark-field scanning transmission electron microscopy (HAADF-STEM) image of the sample thinned to 100 nm thickness. The formation of the 1st to 16th, 24th, and 25th layers could be seen in the order from the sapphire substrate. In addition, voids or low-density regions were observed in the 2nd and 3rd layers. Fig. 6(b) and (c) show energy dispersive X-ray (EDX) and cross-sectional bright-field STEM (BF-STEM) images, respectively. Few dislocations were observed in the 1st layer, but the occurrence of many dislocations was observed starting from the 2nd layer. The dislocation density was estimated to be 7.5 × 10^{10} cm^{-2} in the high-Al-composition region using the Ham method.[44] The EDX analysis reveals that the first and second layers were α-$(Al_{0.96}Ga_{0.04})_2O_3$ and α-$(Al_{0.84}Ga_{0.16})_2O_3$, with a lattice mismatch of about 0.57% along the a-axis. Although this lattice mismatch value is smaller than that between α-Al_2O_3 and α-Ga_2O_3 (about 4.60%), the dislocation density is comparable to that of α-Ga_2O_3 grown directly on a sapphire substrate.[30] This indicates that more smoothly compositionally graded layers may be needed or that it might be hard to drastically reduce dislocation density by compositionally step-graded α-

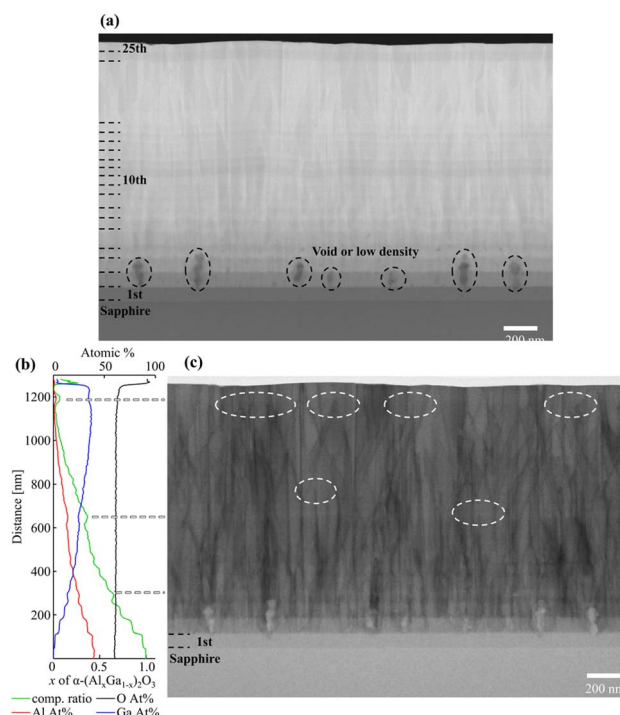**Fig. 5** Reciprocal space mapping around $(10\bar{1},10)$ reflections from compositionally step-graded α-$(Al_xGa_{1-x})_2O_3$ layers.

Fig. 6 Cross-sectional (a) HAADF-STEM and (c) BF-STEM images, and (b) EDX spectra of compositionally step-graded α-$(Al_xGa_{1-x})_2O_3$ layers.

Paper

$(Al_xGa_{1-x})_2O_3$ layers. On the other hand, it was also found that the dislocations were bent and reduced due to being dislocated out of the TEM sample or pair annihilation in the compositionally graded α-$(Al_xGa_{1-x})_2O_3$. The dislocation density in the high-Ga-composition region was determined to be 3.6×10^{10} cm^{-2}, which is approximately half of that in the high-Al-composition region, and is similar to the results reported by B. Kim et al.[37] This indicates that the dislocation can be completely bent in the in-plane direction to eliminate the dislocations in the crystal growing on it, or even if not completely bent, the bending can induce pair annihilation, resulting in a reduction in the dislocation density. Based on the EDX results, the x of α-$(Al_xGa_{1-x})_2O_3$ decreased gradually from the substrate interface. However, there were three areas where it increased and the dislocation bending, dislocation disappearance from the TEM specimen, or pair annihilation occurred in the vicinity of these areas [Fig. 6(b) and (c)]. This indicates that the dislocation can be bent by compositional changes, suggesting that the use of a superlattice buffer, which alternates compressive and tensile strain by changing the composition of the α-$(Al_xGa_{1-x})_2O_3$, may be effective in reducing the dislocation density.

To elucidate the mechanism of dislocation reduction by strained superlattice buffer layers, structures were fabricated with α-Ga_2O_3 inserted in the compositionally step-graded α-$(Al_xGa_{1-x})_2O_3$ buffer layers. Table 3 shows the fabrication conditions. The fabrication conditions for the compositionally step-graded α-$(Al_xGa_{1-x})_2O_3$ layers were identical to those described in Table 2, except for the introduction of four α-Ga_2O_3

layers of 50 nm thickness within the aforementioned step-graded α-$(Al_xGa_{1-x})_2O_3$ layers.

Fig. 7 illustrates the reciprocal space mapping around the $(10\bar{1},10)$ reflection of the sample that was fabricated in accordance with the fabrication condition in Table 3. As in Fig. 5, the ideal peak positions of α-Al_2O_3 and α-Ga_2O_3 are connected by dashed lines. In Fig. 5, the sample exhibited a slight compressive strain in the high-Al-composition region. However, in Fig. 7, it follows the dashed line and was fully relaxed. Conversely, as the Ga composition increased, the α-$(Al_xGa_{1-x})_2O_3$ peak was observed to be situated above and to the left of the dashed line, indicating that it was subjected to tensile strain. Furthermore, the α-Ga_2O_3 peak extended to the lower right side, indicating that it was subjected to compressive strain. The insertion of α-Ga_2O_3 in the compositionally step-graded α-$(Al_xGa_{1-x})_2O_3$ layers resulted in the complete relaxation of the α-$(Al_xGa_{1-x})_2O_3$ layers in proximity to the substrate interface. However, the remaining α-$(Al_xGa_{1-x})_2O_3$ layers were subjected to tensile strain, and the α-Ga_2O_3 layers between the α-$(Al_xGa_{1-x})_2O_3$ layers experienced compressive strain.

Fig. 8(a) and (b) show the results of the EDX analysis and the BF-STEM image respectively. As can be seen in Fig. 8(b), the formation of four α-Ga_2O_3 layers in the step-graded α-$(Al_xGa_{1-x})_2O_3$ layers were confirmed. Region A revealed numerous dislocations were originated from the second layer and were consistent with the observations shown in Fig. 6(c). These findings suggest that up to α-$(Al_{0.96}Ga_{0.04})_2O_3$ can be grown on the c-plane sapphire substrate without the presence of dislocations. In contrast, the formation of voids or low-density areas was observed to be more prevalent than in Fig. 6(c). The dislocation densities of regions A, B, C, D, and the surface α-Ga_2O_3 were estimated to be 6.56×10^{10} cm^{-2}, 6.32×10^{10} cm^{-2}, 5.85×10^{10} cm^{-2}, 5.21×10^{10} cm^{-2}, and 3.71×10^{10} cm^{-2} respectively. The reduction rates were -3.7% for regions A to B, -7.5% for B to C, -10.8% for C to D, and -28.9% for D to surface α-Ga_2O_3 respectively. It is assumed that the smaller compositional alterations were more readily strain without relaxation,

Table 3 Carrier gas conditions of compositionally step-graded α-$(Al_xGa_{1-x})_2O_3$ layers with insertions of α-Ga_2O_3 layers

Layer	Thickness (nm)	Carrier gas flow rate	
		Al (L min^{-1})	Ga (L min^{-1})
1	80	4.8	0.2
2	75	4.6	0.4
3	70	4.4	0.6
4	65	4.2	0.8
5	60	4.0	1.0
6	50	0.0	5.0
7	58	3.8	1.2
8	56	3.6	1.4
9	54	3.4	1.6
10	52	3.2	1.8
11	50	3.0	2.0
12	50	0.0	5.0
13	50	2.8	2.2
	50	**Decrease by 0.2**	**Increase by 0.2**
17	50	2.0	3.0
18	50	0.0	5.0
19	50	1.8	3.2
23	50	1.0	4.0
24	50	0.0	5.0
25	50	0.8	4.2
29	500	0.0	5.0
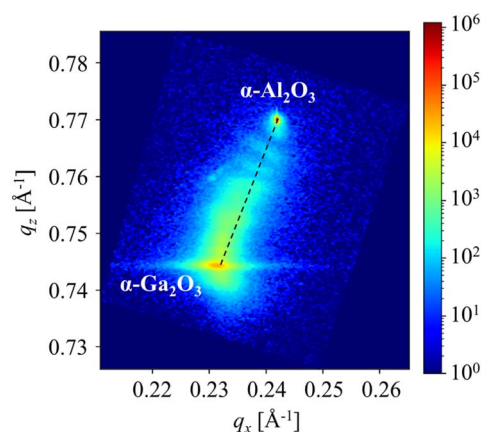
Fig. 7 Reciprocal space mapping around $(10\bar{1},10)$ reflections from compositionally step-graded α-$(Al_xGa_{1-x})_2O_3$ layers with insertions of α-Ga_2O_3 layers.
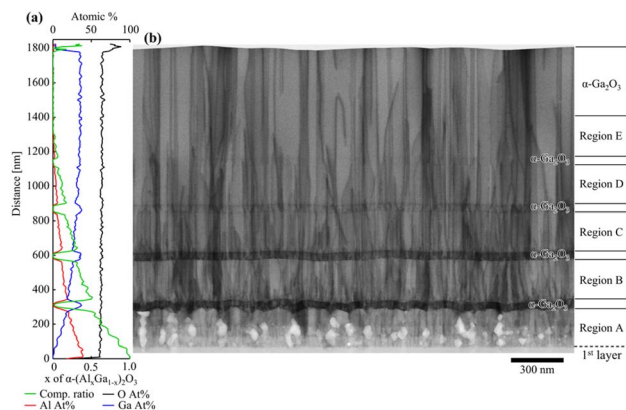
Fig. 8 (a) EDX spectra and (b) cross-sectional BF-STEM image of compositionally step-graded α-(Al$_x$Ga$_{1-x}$)$_2$O$_3$ layers with insertions of α-Ga$_2$O$_3$ layers.

resulting in a greater number of dislocations being bent and thus reducing the number of dislocations.

Fig. 9(a) and (b) show $g/3g$ weak-beam dark-field (WB-DF) images acquired along $\langle 2\bar{1}\bar{1}0 \rangle$ zone axis with diffraction vectors $g = 0\text{--}330$ and $g = 0006$, respectively. In Fig. 9(a), the formation of numerous edge dislocations was confirmed at the interface with the substrate, originating from the second or third layer of step-graded α-(Al$_x$Ga$_{1-x}$)$_2$O$_3$ layers. These dislocations exhibited a gradual decrease after the α-Ga$_2$O$_3$ layers grown between α-(Al$_x$Ga$_{1-x}$)$_2$O$_3$ layers, particularly within regions D and E. In contrast, Fig. 9(b) shows that the formation of screw dislocations originated from the second layer of step graded α-(Al$_x$Ga$_{1-x}$)$_2$O$_3$ layers. However, a comparison between regions A and B suggests more dislocations in Region B. Given that previous research has indicated that the number of screw dislocations in α-Ga$_2$O$_3$ grown directly on sapphire substrates was less than 10^7 cm^{-2},[30] it can be postulated that the screw dislocations were formed by the insertion of α-Ga$_2$O$_3$ layers. However, the number of screw dislocations exhibited a decrease in regions C, D, and E, with the α-Ga$_2$O$_3$ layer serving as the

separation point. In particular, a notable reduction in screw dislocations was observed between regions B and C. This indicates that when the thickness of the α-Ga$_2$O$_3$ layer sandwiched between the α-(Al$_x$Ga$_{1-x}$)$_2$O$_3$ layers is 50 nm, it is effective to apply a smaller composition change, hence, a smaller strain to reduce edge dislocations and a larger composition change, hence, a larger strain to reduce screw dislocations. Although this study only varied the composition of α-(Al$_x$Ga$_{1-x}$)$_2$O$_3$, it would be interesting to investigate how dislocations change when the film is strained by varying the thicknesses of each layer, as this also contributes to the strain. From Fig. 9(a) and (b), the edge dislocation density, screw dislocation density, and mixed dislocation density in the surface α-Ga$_2$O$_3$ layer were estimated to be 1.71×10^{10} cm^{-2}, 5.20×10^9 cm^{-2}, and 1.34×10^{10} cm^{-2} respectively. These values were comparable to those obtained in previous studies utilizing quasi-graded α-(Al$_x$Ga$_{1-x}$)$_2$O$_3$ buffer layers.[36] The quasi-graded buffer layer was composed of multiple layers of two distinct α-(Al$_x$Ga$_{1-x}$)$_2$O$_3$ compositions, exhibiting varying thicknesses. In consideration of the findings of the present study, it can be posited that the dislocation density was decreased as a result of the effective strain for dislocation bending in specific layers of a given thickness. It is expected that further reduction of dislocation density will be achieved in future investigations by optimizing the film thickness and the compositional change of α-(Al$_x$Ga$_{1-x}$)$_2$O$_3$ that applies effective strain to the dislocation bending, as well as by layering multiple layers of these films.

4. Conclusions

In conclusion, compositionally step-graded α-(Al$_x$Ga$_{1-x}$)$_2$O$_3$ layers were grown on a *c*-plane sapphire substrate using mist CVD. Few dislocations were observed in the initial α-(Al$_{0.96}$Ga$_{0.04}$)$_2$O$_3$ layer; however, numerous dislocations were confirmed from the subsequent α-(Al$_{0.84}$Ga$_{0.16}$)$_2$O$_3$ layer. The dislocation density was similar to that of α-Ga$_2$O$_3$ grown directly on sapphire substrates. However, the dislocation density in the high-Ga-composition α-(Al$_x$Ga$_{1-x}$)$_2$O$_3$ layer was decreased by
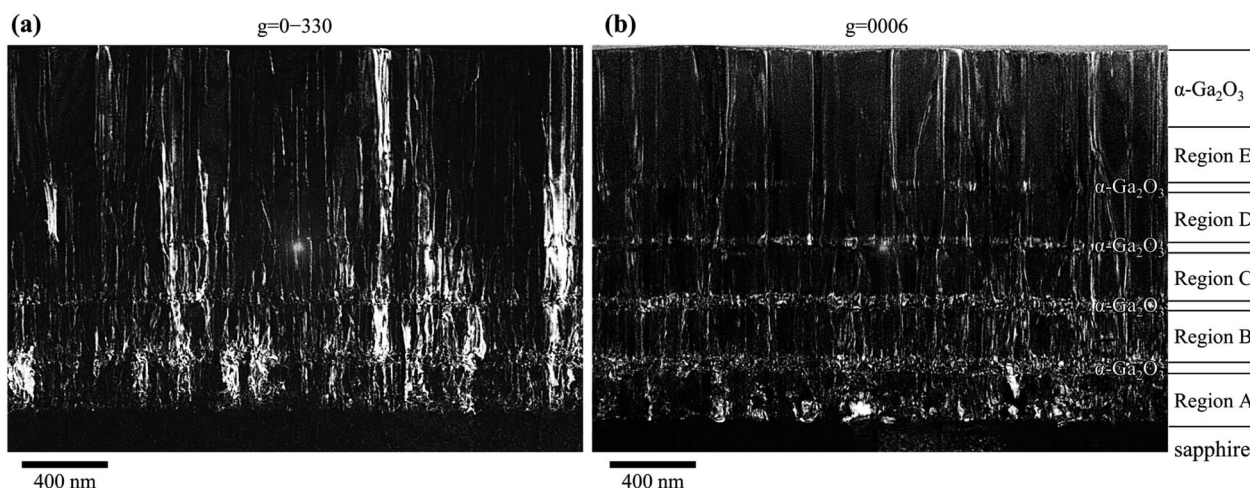

Fig. 9 WB-DF images along $\langle 2\bar{1}\bar{1}0 \rangle$ zone axis with diffraction vector (a) $g = 0\text{--}330$ and (b) $g = 0006$.

approximately 50% due to the dislocation bending in the α-$(Al_xGa_{1-x})_2O_3$ layers. This dislocation bending was observed in the α-$(Al_xGa_{1-x})_2O_3$ layers where alternating compressive and tensile stresses were applied as a result of composition differences. To clarify the mechanism of dislocation bending, compositionally step-graded α-$(Al_xGa_{1-x})_2O_3$ layers inserted with several α-Ga_2O_3 layers was fabricated. The dislocations were reduced following the insertion of α-Ga_2O_3 layers into the compositionally step-graded α-$(Al_xGa_{1-x})_2O_3$. The results of the reciprocal space mapping indicate that this α-Ga_2O_3 layer was strained, and it is proposed that the dislocations are bent by the strain caused by the compositional change of α-$(Al_xGa_{1-x})_2O_3$, resulting in the reduction of dislocations. The differentiation of dislocation types according to the WB-DF images revealed that smaller strains resulting from smaller compositional changes were effective in reducing edge dislocations, whereas larger strains resulting from larger compositional changes were effective in reducing screw dislocations. It is expected that future investigations will achieve a further reduction in dislocation density by optimizing the film thickness and the compositional change of α-$(Al_xGa_{1-x})_2O_3$, which applies effective strain to the dislocation bending. Additionally, the use of multiple layers of these films will be examined as a means of further reducing dislocation density.

Data availability

The data supporting this article is included in the manuscript.

Author contributions

Tatsuya Yasuoka – conceptualization, methodology, investigation, visualization, and writing original draft; Hiromu Susami – investigation; Li Liu – methodology and investigation; Giang T. Dang – methodology and writing review & editing; Toshiyuki Kawaharamura – conceptualization, project administration, supervision, methodology, and writing review & editing.

Conflicts of interest

There are no conflicts to declare.

References

1 H. Y. Playford, A. C. Hannon, E. R. Barney and R. I. Walton, *Chem.–Eur. J.*, 2013, **19**, 2803.
2 M. Orita, H. Ohta, M. Hirano and H. Hosono, *Appl. Phys. Lett.*, 2000, **77**, 4166.
3 T. Onuma, S. Saito, K. Sasaki, T. Masui, T. Yamaguchi, T. Honda and M. Higashiwaki, *Jpn. J. Appl. Phys.*, 2015, **54**, 112601.
4 A. B. Chase, *J. Am. Ceram. Soc.*, 1964, **47**, 470.
5 A. Kuramata, K. Koshi, S. Watanabe, Y. Yamaoka, T. Masui and S. Yamakoshi, *J. Appl. Phys.*, 2016, **55**, 1202A2.
6 K. Hoshikawa, E. Ohba, T. Kobayashi, J. Yanagisawa, C. Miyagawa and Y. Nakamura, *J. Cryst. Growth*, 2016, **447**, 36.
7 Z. Galazka, R. Uecker, D. Klimm, K. Irmscher, M. Naumann, M. Pietsch, A. Kwasniewski, R. Bertram, S. Ganschow and M. Bickermann, *ECS J. Solid State Sci. Technol.*, 2017, **6**(2), Q3007.
8 K. Sasaki, A. Kuramata, T. Masui, E. G. Víllora, K. Shimamura and S. Yamakoshi, *Appl. Phys. Express*, 2012, **5**, 035502.
9 G. Wagner, M. Baldini, D. Gogova, M. Schmidbauer, R. Schewski, M. Albrecht, Z. Galazka, D. Klimm and R. Fornari, *Phys. Status Solidi A*, 2014, **211**(1), 27.
10 H. Murakami, K. Nomura, K. Goto, K. Sasaki, K. Kawara, Q. Tu Thieu, R. Togashi, Y. Kumagai, M. Higashiwaki, A. Kuramata, S. Yamakoshi, B. Monemar and A. Koukitu, *Appl. Phys. Express*, 2015, **8**, 015503.
11 D. Shinohara and S. Fujita, *Jpn. J. Appl. Phys.*, 2008, **47**, 7311.
12 A. Segura, L. Artús, R. Cuscó, R. Goldhahn and M. Feneberg, *Phys. Rev. Mater.*, 2017, **1**, 024604.
13 D. Shinohara, H. Nishinaka, T. Ohshima, K. Kiba, Y. Kamada, T. Kawaharamura, and S. Fujita, *The 55th JSAP Spring Meeting*, 28a-W-2, 2008.
14 T. Wakamatsu, H. Takane, K. Kaneko, T. Araki and K. Tanaka, *Jpn. J. Appl. Phys.*, 2023, **62**, SF1024.
15 Y. Oshima, E. G. Víllora and K. Shimamura, *Appl. Phys. Express*, 2015, **8**, 055501.
16 K. Goto, H. Nakahata, H. Murakami and Y. Kumagai, *Appl. Phys. Lett.*, 2020, **117**, 222101.
17 Z. Cheng, M. Hanke, P. Vogt, O. Bierwagen and A. Trampert, *Appl. Phys. Lett.*, 2017, **111**, 162104.
18 A. F. M. A. U. Bhuiyan, Z. Feng, H. L. Huang, L. Meng, J. Hwang and H. Zhao, *APL Mater.*, 2021, **9**, 101109.
19 G. T. Dang, T. Yasuoka, Y. Tagashira, T. Tadokoro, W. Theiss and T. Kawaharamura, *Appl. Phys. Lett.*, 2018, **113**, 062102.
20 G. T. Dang, S. Sato, Y. Tagashira, T. Yasuoka, L. Liu and T. Kawaharamura, *APL Mater.*, 2020, **8**, 101101.
21 R. Jinno, K. Kaneko and S. Fujita, *Jpn. J. Appl. Phys.*, 2021, **60**, SBBD13.
22 R. Jinno, C. S. Chang, T. Onuma, Y. Cho, S. T. Ho, D. Rowe, M. C. Cao, K. Lee, V. Protasenko, D. G. Schlom, D. A. Muller, H. G. Xing and D. Jena, *Sci. Adv.*, 2021, 7(2), eabd5891.
23 T. Uchida, R. Jinno, S. Takemoto, K. Kaneko and S. Fujita, *Jpn. J. Appl. Phys.*, 2018, **57**, 040314.
24 G. T. Dang, Y. Tagashira, T. Yasuoka, L. Liu and T. Kawaharamura, *AIP Adv.*, 2020, **10**, 115019.
25 N. Suzuki, K. Kaneko and S. Fujita, *J. Cryst. Growth*, 2014, **401**, 670.
26 K. Kaneko, T. Nomura, I. Kakeya and S. Fujita, *Appl. Phys. Express*, 2009, **2**, 075501.
27 K. Kaneko, T. Nomura and S. Fujita, *Phys. Status Solidi C*, 2010, **7**, 2467.
28 K. Kaneko, Y. Masuda, S. I. Kan, I. Takahashi, Y. Kato, T. Shinohe and S. Fujita, *Appl. Phys. Lett.*, 2021, **118**, 102104.
29 R. Schewski, G. Wagner, M. Baldini, D. Gogova, Z. Galazka, T. Schulz, T. Remmele, T. Markurt, H. Von Wenckstern, M. Grundmann, O. Bierwagen, P. Vogt and M. Albrecht, *Appl. Phys. Express*, 2015, **8**, 011101.
30 K. Kaneko, H. Kawanowa, H. Ito and S. Fujita, *Jpn. J. Appl. Phys.*, 2012, **51**, 020201.

31 T. C. Ma, X. H. Chen, Y. Kuang, L. Li, J. Li, F. Kremer, F. F. Ren, S. L. Gu, R. Zhang, Y. D. Zheng, H. H. Tan, C. Jagadish and J. D. Ye, *Appl. Phys. Lett.*, 2019, **115**, 182101.

32 Y. Oshima, K. Kawara, T. Shinohe, T. Hitora, M. Kasu and S. Fujita, *APL Mater.*, 2019, **7**, 022503.

33 G. T. Dang, T. Yasuoka and T. Kawaharamura, *Appl. Phys. Lett.*, 2021, **119**, 041902.

34 R. Jinno, N. Yoshimura, K. Kaneko and S. Fujita, *Jpn. J. Appl. Phys.*, 2019, **58**, 120912.

35 Y. Oshima, H. Ando and T. Shinohe, *Appl. Phys. Express*, 2023, **16**, 065501.

36 R. Jinno, T. Uchida, K. Kaneko and S. Fujita, *Appl. Phys. Express*, 2016, **9**, 071101.

37 B. Kim, D. Yang, W. Sohn, S. Lee, H. H. C. Choi, T. Jang, E. Yoon, Y. Park and H. W. Jang, *Acta Mater.*, 2021, **221**, 117423.

38 T. Kawaharamura, *Jpn. J. Appl. Phys.*, 2014, **53**, 05FF08.

39 T. Kawaharamura, M. Nishi, L. Liu, P. Rutthongjan, Y. Ishikawa, M. Sakamoto, T. Yasuoka, K. Asako, T. Ozaki, M. Fukue, M. Ueda, S. Sato and G. T. Dang, *Jpn. J. Appl. Phys.*, 2024, **63**, 015502.

40 L. Liu, T. Kawaharamura, G. T. Dang, E. K. C. Pradeep, S. Sato, T. Uchida, S. Fujita, T. Hiramatsu, H. Kobayashi and H. Orita, *Jpn. J. Appl. Phys.*, 2019, **58**, 025502.

41 P. Rutthongjan, M. Nishi, L. Liu, S. Sato, Y. Okada, G. T. Dang and T. Kawaharamura, *Appl. Phys. Express*, 2019, **12**, 065505.

42 P. Rutthongjan, L. Liu, M. Nishi, M. Sakamoto, S. Sato, E. K. C. Pradeep, G. T. Dang and T. Kawaharamura, *Jpn. J. Appl. Phys.*, 2019, **58**, 035503.

43 M. Oda, K. Kaneko, S. Fujita and T. Hitora, *Jpn. J. Appl. Phys.*, 2016, **55**, 1202B4.

44 R. K. Ham, *Philos. Mag.*, 1961, **6**, 1183.